Modeling and testing of the collective effects of thermoelastic and fluid damping on silicon MEMS resonators

Yun-Bo Yi
University of Denver
Department of Mechanical and Materials Engineering
Denver, Colorado 80208
E-mail: yyi2@du.edu

Amir Rahafrooz
Siavash Pourkamali
University of Denver
Department of Electrical and Computer Engineering
Denver, Colorado 80208

Abstract. Thermoelastic damping and fluid damping may collectively affect the resonant behaviors of silicon resonators. A finite element model is developed to predict the characteristics of the out-of-plane resonance, and the results are verified by experiments. The implementation of the perturbation method leads to an eigenvalue equation, from which the resonant frequency and the quality factor can be evaluated. The fluid damping problem is formulated by augmenting the governing equation with a linear damping term, whose coefficient is inversely determined from the experimental correlations. With the incorporation of the fluid damping term, the computational prediction achieves a good agreement with the experiment. The same method can also be extended to study the in-plane vibration of beam resonators. © *2009 Society of Photo-Optical Instrumentation Engineers.* [DOI: 10.1117/1.3129830]

Subject terms: simulations; vibration analysis; sensors.

Paper 09006R received Jan. 16, 2009; revised manuscript received Mar. 17, 2009; accepted for publication Mar. 24, 2009; published online May 4, 2009.

1 Introduction

Various energy dissipation mechanisms exist in microelectromechanical systems (MEMS) and nanoelectromechanical systems (NEMS). These mechanisms include viscous effects,[1] anchor losses,[2] squeeze film damping,[3] nonlinear acoustic effects,[4] and thermoelastic damping.[5]

Thermoelastic damping involves the coupling between thermoelasticity and structural dynamics, and it is strongly evident that this mechanism is a dominant source of intrinsic damping in MEMS and NEMS resonators operating at high frequencies.[5] The earliest work related to thermoelastic damping can be traced back to Zener,[6] who established a general theory of thermoelastic damping and derived an approximation equation to relate the energy dissipation. Lifshitz and Roukes[7] later improved the method and derived an exact solution for the same problem from the equations of motion and thermoelasticity. Nayfeh and Younis[8] derived an analytical solution for the problem involving microplates of finite width. The same analytical approaches were also successfully applied to other geometries, including thin rings[9,10] as well as circular thin-plate resonators.[11,12]

The implementation of the finite element scheme on the formulation of thermoelastic damping[13,14] leads to a more efficient tool when the system has a complex geometry or nonhomogeneous boundaries. Yi's group further improved this method for beams,[15] plates,[16] and axisymmetric rings[17] and derived a generalized eigenvalue scheme for the problem based on the Fourier reduction.[18] The method was analogous to the formulation of thermoelastodynamic instability (TEDI) in automotive applications[19] and was successfully implemented to solve the resonator damping problems involved in both two-dimensional (2-D) and three-dimensional (3-D) structures.

On the other hand, fluid damping, which may include both viscous damping and squeeze film damping, is also an important damping mechanism for resonators operating in viscous fluid, such as air and water. The resonance characteristics of MEMS under fluid damping have been investigated by several research groups. For example, Basak et al.[20] developed a fully 3-D finite element–based fluid structure interaction model to predict the hydrodynamic loading of microcantilevers in viscous fluids. Inaba et al.[21] analyzed the resonant frequency of a cantilever vibrated photothermally in water and compared the experimental results with the theoretical predictions. Naik et al.[22] investigated the effects of liquid properties and gap height on the dynamic response of a resonant cantilever in terms of added mass and viscous damping coefficient. A more comprehensive work, which integrated the coupling of hierarchical fluid models with electrostatic and mechanical models for MEMS, was carried out by De and Aluru.[23] Hao et al.[24] investigated the air damping effect in a bulk micromachined tilt mirror by using both the analytical and numerical methods.

However, the computational models developed in the preceding research were predominantly based on the transient solution scheme, which requires a very small time step in the presence of fluid damping. This typically results in very intensive numerical iterations. In addition, the mode patterns altered by the shear tractions of viscous fluid may impose additional constraints on the heat flow induced by thermoelastic damping. This will lead to a feedback loop between the two damping mechanisms. A detailed explanation of this coupling process is not yet known.

Here, we seek a methodology that leads to a computa-

1932-5150/2009/$25.00 © 2009 SPIE

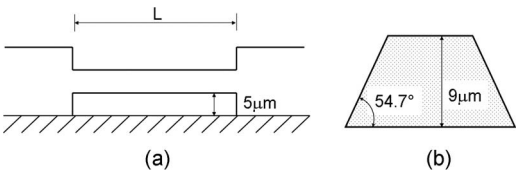

Fig. 1 Schematic of the beam structure under investigation: (a) side view; (b) cross section.

tionally reduced model and that can be used to investigate the collective effect of thermoelastic damping and fluid damping in resonator systems. This requires the linearization of the governing heat transfer and dynamics equations as well as the formulation of an eigenvalue equation from which the resonance characteristics can be predictively modeled.

2 Experimental Procedure

The fabrication process sequence of the required MEMS resonators is shown in Fig. 1. The resonator structure is first defined by selective anisotropic etching of the device silicon layer in an aqueous potassium hydroxide (KOH) solution. This anisotropic etching resulted in a 54.7-deg angle for the etched sidewalls, defined by the crystalline structure of the utilized (100) silicon wafers. A thin (~100 nm) thermally grown layer of silicon dioxide was used as the mask in this step. The beams were then undercut and released in hydrofluoric acid (HF) by etching the underlying silicon dioxide. The entire fabrication process is shown schematically in Fig. 2.

Beam resonators with different dimensions were fabricated on silicon-on-insulator (SOI) substrates with different device layer thicknesses. Figure 3 shows the scanning electron microscope (SEM) view of a fabricated 100-μm-long, 20-μm-wide (on top), and 9-μm-thick beam resonator with a 500-nm capacitive transduction gap. The capacitive transduction gap lies between the silicon handle layer of the SOI substrate and the beam carved in the SOI device layer. Therefore, the size of the gap is determined by the thickness of the buffer oxide (BOX) layer of the starting SOI

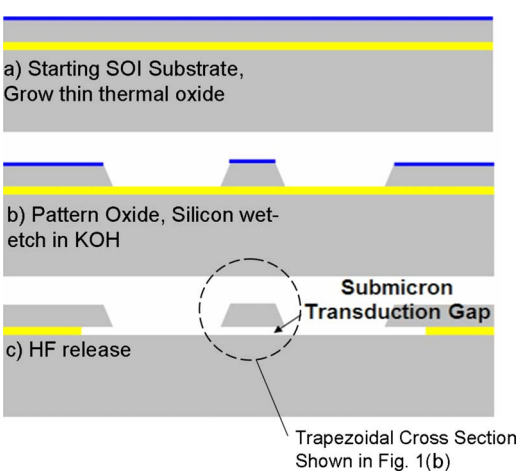

Fig. 2 Process flow used for fabrication of the beam resonators.

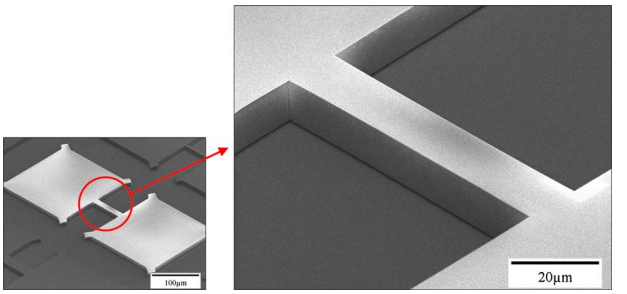

Fig. 3 SEM image of the experimental setup of a MEMS beam resonator with a 0.5-μm transduction gap.

substrate and can be much smaller than the lithography limits (potentially as small as a few nanometers).

To measure the resonant properties, the fabricated beam resonators were operated in a one-port configuration in which the SOI handle layer acted as the actuation electrode. A DC bias voltage (V_{bias}) in addition to the AC actuation signal from the network analyzer were applied to the handle layer while the output current was collected from the resonator body. To separate the DC and AC paths to the power supplies, the DC bias was applied through a large resistor (100 kΩ) and the AC signal was applied through a relatively large capacitor (1 μF).

The fluctuating electrostatic force applied by the substrate to the beam structure caused vertical (out of plane) mechanical vibrations in the beam that were amplified at their mechanical resonant frequencies (2 to 6 MHz in this work, depending on the beam dimensions). The current induced in the beam is a function of the DC bias voltage and the vibration amplitude of the resonator. The frequency response of the resonators was measured by connecting the resonator body to the input of a network analyzer that measured and graphed the resulting output current as a function of frequency.

3 Computational Method

3.1 *Analytical Approach*

Lifshitz and Roukes[7] derived a closed form solution for the thermoelastic damping effect on beam resonators, shown here:

$$Q = \frac{\rho C_p \xi^2}{6E\alpha^2 T_0 \left[1 - \dfrac{\sin\xi + \sinh\xi}{\xi(\cos\xi + \cosh\xi)}\right]}, \tag{1}$$

where

$$\xi = h\left(\frac{\omega_0}{2\kappa}\right)^{1/2}. \tag{2}$$

Q is the quality factor, ρ is the material density, α is the thermal expansion coefficient, C_p is the specific heat capacity, T_0 is the mean temperature, h is the beam thickness, and κ is the thermal diffusivity. For a simple beam system, the first undamped natural frequency is

$$\omega_0 = \beta\left(\frac{Eh^2}{12\rho L^4}\right)^{1/2}, \tag{3}$$

where β is a coefficient determined by the boundary constraints, E is Young's modulus, and L is the beam length. The value of β is π^2, 3.52, 22.4 for simply supported, cantilever, and clamped-clamped conditions, respectively.[25] Setting

$$\frac{\partial Q}{\partial \xi} = 0, \tag{4}$$

yields $-3\xi(\cos\xi+\cosh\xi)^2+3(\sin\xi+\sinh\xi)(\cos\xi+\cosh\xi)+\xi(\sinh^2\xi-\sin^2\xi)=0$, which gives $\xi=2.2246$. This corresponds to the lowest Q factor:

$$Q_{\min} = \frac{2.0236\rho c_p}{E\alpha^2 T_0}. \tag{5}$$

3.2 *Finite Element Formulation for Thermoelastic Damping*

For a two-dimensional (2-D) beam structure, the heat conduction process with thermoelastic damping is governed by the following differential equation:

$$\kappa\left(\frac{\partial^2 T}{\partial x^2}+\frac{\partial^2 T}{\partial y^2}\right) = \frac{\partial T}{\partial t}+\frac{\eta T_0}{\rho C_p}\frac{\partial \bar{\varepsilon}}{\partial t}, \tag{6}$$

where $\bar{\varepsilon}$ is the dilatation strain or the "bulk strain" defined by

$$\bar{\varepsilon} = \varepsilon_x + \varepsilon_y + \varepsilon_z, \tag{7}$$

in which ε_x, ε_y, and ε_z are the strain components in the x, y, and z directions, respectively. η is a term related to the thermal expansion, which can be expressed as

$$\eta = \begin{cases} \dfrac{E\alpha}{(1-2\nu)}, & \text{plain-strain} \\ \dfrac{E\alpha}{(1-\nu)}, & \text{plain-stress} \end{cases}, \tag{8}$$

where ν is Poisson's ratio of the material. The equations of motion for a 2-D elastic body are given here:

$$\frac{\partial \sigma_{xx}}{\partial x}+\frac{\partial \sigma_{xy}}{\partial y} = \rho\frac{\partial^2 u_x}{\partial t^2}, \tag{9}$$

$$\frac{\partial \sigma_{yy}}{\partial y}+\frac{\partial \sigma_{xy}}{\partial x} = \rho\frac{\partial^2 u_y}{\partial t^2}. \tag{10}$$

In the preceding equations, σ_{xx}, σ_{xy}, and σ_{yy} represent the components of stress tensors, and, u_x and u_y are the components of displacement vectors. The constitutive law of thermoelasticity can be written as

$$\begin{Bmatrix}\sigma_{xx}\\ \sigma_{yy}\\ \sigma_{xy}\end{Bmatrix} = \mathbf{C}\begin{Bmatrix}\varepsilon_{xx}\\ \varepsilon_{yy}\\ \varepsilon_{xy}\end{Bmatrix} - \mathbf{D}T, \tag{11}$$

where for plain strain,

$$\mathbf{C} = \frac{E}{(1+\nu)(1-2\nu)}\begin{bmatrix}1-\nu & \nu & 0\\ \nu & 1-\nu & 0\\ 0 & 0 & 1/2-\nu\end{bmatrix}, \tag{12}$$

and for plain stress,

$$\mathbf{C} = \frac{E}{(1-\nu^2)}\begin{bmatrix}1 & \nu & 0\\ \nu & 1 & 0\\ 0 & 0 & (1-\nu)/2\end{bmatrix}. \tag{13}$$

In both cases,

$$\mathbf{D} = \begin{bmatrix}\eta\\ \eta\\ 0\end{bmatrix}. \tag{14}$$

Assume that there exists a perturbation solution of the form

$$\begin{cases} T = \Re\{e^{bt}\Theta\} \\ u = \Re\{e^{bt}U\} \\ \dfrac{\partial u}{\partial t} = \Re\{e^{bt}V\} \end{cases}, \tag{15}$$

where b is a complex exponential growth rate, and $\Re$ represents the real part of a complex number. Applying the standard Galerkin finite element formulation results in two matrix equations in the following form:

$$(\mathbf{K}+b\mathbf{H})\mathbf{\Theta}+b\mathbf{F}\mathbf{U} = \mathbf{0}, \tag{16}$$

and

$$\mathbf{L}\mathbf{U}-\mathbf{G}\mathbf{\Theta}+b\mathbf{M}\mathbf{V} = \mathbf{0}, \tag{17}$$

where $\mathbf{K}$, $\mathbf{H}$, $\mathbf{F}$, $\mathbf{L}$, $\mathbf{G}$, and $\mathbf{M}$ are coefficient matrices determined by the material properties and the shape functions. (see Ref. 15 for the detailed integral expressions for these matrices.) $\mathbf{\Theta}$, $\mathbf{U}$, and $\mathbf{V}$ represent the nodal values of T, U, and V.

Note that there exists an additional relationship between the displacement and velocity perturbations, shown here:

$$\mathbf{V} = b\mathbf{U}. \tag{18}$$

Combining Eqs. (16)–(18) yields

$$\left\{\begin{bmatrix}\mathbf{K} & 0 & 0\\ \mathbf{G} & -\mathbf{L} & 0\\ 0 & 0 & \mathbf{I}\end{bmatrix} - b\begin{bmatrix}\mathbf{H} & \mathbf{F} & 0\\ 0 & 0 & \mathbf{M}\\ 0 & \mathbf{I} & 0\end{bmatrix}\right\}\begin{bmatrix}\mathbf{\Theta}\\ \mathbf{U}\\ \mathbf{V}\end{bmatrix} = 0, \tag{19}$$

or

$$(\tilde{\mathbf{A}}-\mathbf{b}\tilde{\mathbf{B}})\Psi = 0, \tag{20}$$

where

$$\tilde{\mathbf{A}} = \begin{bmatrix} \mathbf{K} & 0 & 0 \\ \mathbf{G} & -\mathbf{L} & 0 \\ 0 & 0 & \mathbf{I} \end{bmatrix}; \quad \tilde{\mathbf{B}} = \begin{bmatrix} \mathbf{H} & \mathbf{NF} & 0 \\ 0 & 0 & \mathbf{M} \\ 0 & \mathbf{I} & 0 \end{bmatrix}; \quad \Psi = [\Theta, \mathbf{U}, \mathbf{V}]^T, \tag{21}$$

and $\mathbf{I}$ is an identity matrix. This is a generalized eigenvalue equation in which the eigenvalue is the growth rate b and the eigenvector is $[\mathbf{\Theta}, \mathbf{U}, \mathbf{V}]^T$, i.e., the nodal temperature, displacement, and velocity.

The quality factor Q defines the attenuation of the resonance and is determined by

$$Q = \frac{1}{2}\left|\frac{\Im(b)}{\Re(b)}\right|, \tag{22}$$

where $\Re(b)$ and $\Im(b)$ represent the real part and the imaginary part of the growth rate b, respectively.

3.3 *Finite Element Formulation of Collective Thermoelastic and Fluid Damping Effects*

The fluid drag acting on the beam resonator is caused by the skin friction force and the pressure drop in the fluid flow. For laminar flow over the thickness direction of beam, the friction drag coefficient is determined by

$$C_D = \frac{F_D}{\frac{1}{2}\rho_f V_y^2 A} = \frac{1.33}{\sqrt{R_e}}, \tag{23}$$

where C_D is the drag coefficient, F_D is the drag force, V_y is the velocity component in the y direction, ρ_f is the fluid density, A is the surface area, and R_e is the Reynolds number.[26] It can be proved that the equivalent shear stress τ_f imposed on the 2-D model is determined by

$$\tau_f = 1.33\rho^{1/2} V_y^{3/2} h^{1/2} \mu^{1/2} w^{-1}, \tag{24}$$

where μ is the fluid dynamic viscosity, h is the beam thickness, and w is the beam width. For the out-of-plane motion of the beam, however, the velocity is orthogonal to the beam width, and therefore the pressure drag should be dominant. From the momentum consideration, we know that

$$\tau_p \propto \rho V_y^2. \tag{25}$$

Here, we manage to linearize the fluid damping term by assuming that

$$\tau = \tau_f + \tau_p \approx \lambda V_y, \tag{26}$$

where λ is a coefficient determined by various parameters including the fluid properties, the beam aspect ratio, and the beam velocity components. Although the dependence of the shear tractions on the velocity are nonlinear, as shown in Eqs. (24) and (25), in the vicinity of the equilibrium state, we may linearize the problem so that the eigenvalue scheme can be implemented. To fully incorporate the nonlinear effects, one must resort to the transient simulation in the time domain, which would be computationally prohibitive.

According to Eq. (25) and considering that τ_p is a dominant term here, λ should be approximately proportional to the mean beam velocity $\bar{V}_y$, which is related to the product of the resonant amplitude and the resonant frequency. From the fundamental beam theory, the deflection of a horizontal beam subjected to a uniform vertical traction is given by

$$d \propto \frac{L^4}{h^3}. \tag{27}$$

From Eq. (3), we know the resonant frequency:

$$\omega_0 \propto \frac{h}{L^2}. \tag{28}$$

Therefore,

$$\lambda \propto \frac{L^2}{h^2}, \tag{29}$$

and we need to modify Eq. (26) as

$$\tau = \gamma \frac{L^2}{h^2} V_y, \tag{30}$$

where γ is a nonlinear function of the beam width w as well as the boundary conditions and other factors. A theoretical derivation of the analytical expression of γ will be difficult, and therefore in the present study, we inversely determine its value from the experimental correlations. The determined γ can then be used for predictions of resonant properties for beams operating in other conditions.

Once the fluid damping coefficient γ in Eq. (30) is known, the external traction τ can be incorporated into the equation of motion, and the resulting matrix equation will reflect the fluid damping effect. Particularly, Eq. (17) should be modified as the following form:

$$\mathbf{LU} - \mathbf{G\Theta} + b\mathbf{MV} + \mathbf{PV} = \mathbf{0}, \tag{31}$$

where $\mathbf{P}$ is the fluid damping coefficient matrix, whose elemental matrix is given by the following integral expression:

$$\mathbf{P_e} = \int_\Omega \gamma \frac{L^2}{h^2} \mathbf{N}\mathbf{N}^T \mathrm{d}x\, \mathrm{d}y, \tag{32}$$

where $\mathbf{N}$ is the shape function. Accordingly, the eigenvalue (19) should be modified as

$$\left\{ \begin{bmatrix} \mathbf{K} & 0 & 0 \\ \mathbf{G} & -\mathbf{L} & \mathbf{P} \\ 0 & 0 & \mathbf{I} \end{bmatrix} - b \begin{bmatrix} \mathbf{H} & \mathbf{F} & 0 \\ 0 & 0 & \mathbf{M} \\ 0 & \mathbf{I} & 0 \end{bmatrix} \right\} \begin{bmatrix} \mathbf{\Theta} \\ \mathbf{U} \\ \mathbf{V} \end{bmatrix} = 0, \tag{33}$$

to incorporate the fluid damping term.

4 Results

4.1 *Analytical Solutions versus Finite Element Results*

To validate the finite element method, the eigenfrequency and the Q factor were obtained and compared to the analytical solutions. The analysis was performed using the 2-D

Table 1 Silicon properties used in the models.

Young's modulus, E (Pa)	1.31×10^{11}
Poisson's ratio	0.27
Thermal expansion coefficient, α (K^{-1})	4.15×10^{-6}
Thermal conductivity, k (W/m·K)	163
Specific heat (J/Kg·K)	703
Density, ρ (kg/m^3)	2330
Temperature (K)	300

quadrilateral plane-strain elements as formulated earlier. The silicon material properties were retrieved from the COMSOL materials library[27] and are listed in Table 1. The beam length was discretized into 100 elements in the model to prevent shear locking of the bending performance. Meanwhile, 10 elements were used in the thickness direction. Increasing the element number beyond these values has proved difficult due to the computer capacity available. The analytical solution for the first natural frequency of the beam was computed using Eq. (3). According to the computational results presented in Table 2 and Fig. 4, it is seen that the analytical and numerical solutions agree very well in most situations. For the beam length below 50 microns, the discrepancy is relatively significant, because the analytical solution was derived from the beam theory, which is inapplicable to short beams. It is also found that changing Poisson's ratio of the material (ν=0 versus ν=0.27) does not affect the resonant frequency very much.

Comparisons of the Q factor also reveal that the analytical solution and the finite element result agree very well when Poisson's ratio is set to zero (see Fig. 5). When a realistic Poisson's ratio (ν=0.27) is used, however, the discrepancy is quite significant. This is because Lifshitz's solution does not include the shear stress effects induced by a nonzero Poisson's ratio. Consequently, the quality factor is underestimated. Despite the different Q values predicted, the beam length associated with the minimum Q is consistent among these models, which stays in the vicinity of 180 μm.

Table 2 Comparisons of resonant frequency between experiments and theoretical predictions.

Beam length (μm)	Finite element frequency (MHz)	Analytical solution frequency (MHz)	Test frequency (MHz)
100	6.915	6.945	5.438±0.149
150	3.17	3.087	2.679±0.055
200	1.810	1.737	1.615±0.070

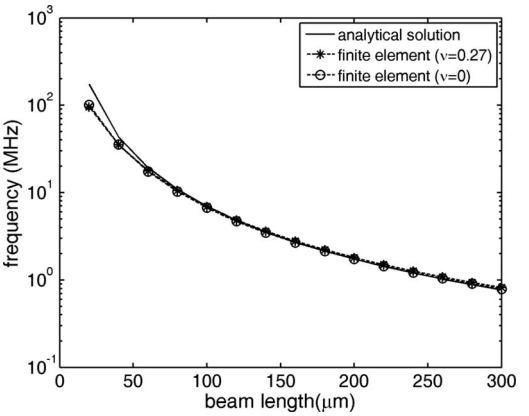

Fig. 4 Comparisons between the finite element solutions and the analytical solutions for the resonant frequency.

4.2 *Correlations between Experiments and Computational Results*

Comparisons between the experiment results and the preceding theoretical predictions in Table 3 show that the resonant frequency can be predicted with good accuracy by either the analytical formula or the finite element analysis. According to the same table, when the beam lengths are 100, 150, and 200 μm, the finite element model predicts resonant frequencies of 6.915, 3.17, and 1.810 MHz, respectively. Meanwhile, the test results are 5.438, 2.679, and 1.615 MHz, respectively. The test results have been averaged over the beams with various widths from 15 to 20 μm, and both the mean values and the standard deviations are reported in the same table. The discrepancy between the experiments and the theoretical predictions could be caused by the following reasons:

1. The cross section of the beam sample is trapezoidal instead of a rectangular shape assumed in the model.
2. A 2-D geometry is assumed, whereas the real device has a finite width, which may impose nonnegligible boundary constraint across the transverse direction.
3. The realistic boundary constraints at the two ends are

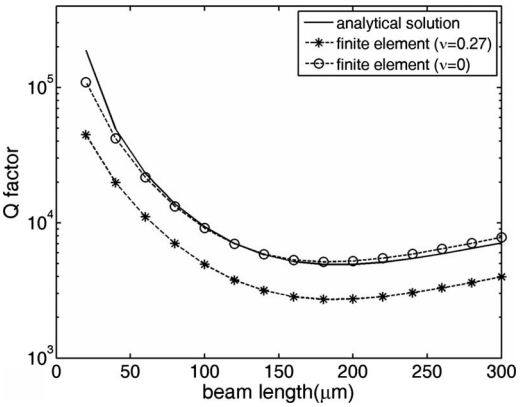

Fig. 5 Comparisons between the finite element solutions and the analytical solutions (without involving fluid damping) for the quality factor.

Table 3 Comparisons of quality factor between experiments and theoretical predictions.

Beam length (μm)	Beam width (μm)	Experiment Q factor	γ	Predicted Q based on averaged γ
100	20	295	9.96	423
100	10	232	12.7	281
100	5	174	17.4	175
100	2	122	24.9	116
100	1.5	104	29.5	91.7
150	20	116	5.27	91.4
150	10	66	9.48	59.6
150	5	40	15.8	36.5
150	2	22	28.8	24.0
150	1.5	21	30.1	18.9
200	20	40	5.10	30.2
200	10	22	9.32	19.5
200	5	11	18.6	11.9
200	2	8	25.6	7.78
200	1.5	5	41.0	6.13

more complicated than the clamped-clamped assumption.

4. There is an inaccuracy in measuring the beam parameters—for instance, the measurement tolerance of the beam thickness turns out to be ± 0.5 micron, which could result in an error of $\pm 6\%$ for the computed resonant frequency.
5. The material properties assumed in the model may not be exact. Despite the discrepancy, the predicted results are not far from the test data and should be considered acceptable. The maximum deviation of the predicted values is around 12% to 27% in comparison with the test result, with a longer beam yielding a smaller error.

For the quality factor, however, the original model would not make good predictions if the fluid damping term were not included. In fact, the predicted Q factor is about one or two orders of magnitude higher than the experimental results (compare Fig. 5 and the third column in Table 3). This implies that the fluid damping, rather than thermoelastic damping, is a dominant damping source in these tests. To include the fluid damping effects, the damping coefficient γ in Eq. (30) was estimated in each experiment, and the results were then averaged over all three beam lengths for each beam width. (Note that γ is independent of beam length or beam thickness.) The correlation results are detailed in Tables 3 and 4. In Table 3, the γ value was computed for each test based on the finite element analysis. These values were averaged to obtain the mean γ for each of the beam widths, as shown in Table 4, which in turn predicts the Q factors for different beam lengths, as shown in the last column of Table 3. According to Table 4, it is seen that the correlated γ shows small variations among the different beam lengths. For example, $\gamma=17.3$ with a standard deviation of 1.43 is obtained for beam width of 5 μm, indicating that Eq. (30) is a good fit for the fluid damping term in the problem of interest. The averaged damping coefficient is then used to compute the quality factor for different beam lengths and widths, and the results are shown in Fig. 6. Clearly, the experiments and the fluid damping model achieve good agreements.

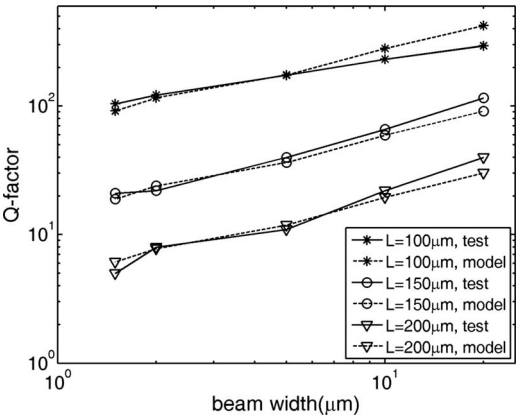

Fig. 6 Comparisons between the experiments and computational results using the fitted fluid damping coefficient.

5 Conclusions

The combined effect of thermoelastic damping and fluid damping was investigated both numerically and experimentally using a silicon MEMS beam resonator. By applying a small perturbation, the governing differential equations were converted to an eigenvalue equation, in which the eigenvalue contains the growth rate leading to the frequency and quality factor of resonance. The finite element method was applied to obtain approximation solutions with

Table 4 Determination of fluid damping coefficient γ.

Beam width (μm)	20	10	5	2	1.5
Averaged γ	6.78±2.76	10.5±1.92	17.3±1.43	26.4±2.04	33.5±6.46

or without the presence of the fluid damping terms separately. The results obtained from the model were compared to the experiments in which a clamped-clamped beam resonates vibrated in air. It is shown that the predicted quality factor using a thermoelastic damping model alone is much higher than the test results, indicating that the fluid damping is the dominant damping source for the resonant system of interest. Good correlations were achieved by the linearization of the governing equations and by the introduction of the fluid damping coefficient, whose value was inversely determined from the experiments. The methodology can be extended to other situations in which the beam has a different size scale or a different geometric shape, or in a situation where the thermoelastic damping is equally important (which is likely to occur when the beam size approaches to nanoscale). Future numerical and experimental work may include the incorporation of the lateral traction induced by the in-plane vibration of the resonator, which is believed to have a much lower energy dissipation rate than the out-of-plane motion.

References

1. D. Homentcovschi and R. N. Miles, "Viscous damping of perforated planar micromechanical structures," *Sens. Actuators, A* **119**, 544–552 (2005).
2. Y. H. Park and K. C. Park, "High-fidelity modeling of MEMS resonators—Part 1: anchor loss mechanisms through substrate," *J. Microelectromech. Syst.* **13**, 238–247 (2004).
3. P. Y. Kwok, M. S. Weinberg, and K. S. Breuer, "Fluid effects in vibrating micromachined structures," *J. Microelectromech. Syst.* **14**, 770–781 (2005).
4. R. Vinokur, "Vibroacoustic effects in MEMS," *Sound Vib.* **37**, 22–26 (2003).
5. S. Evoy, A. Olkhovets, L. Sekaric, J. M. Parpia, H. G. Craighead, and D. W. Carr, "Temperature-dependent internal friction in silicon nanoelectromechanical systems," *Appl. Phys. Lett.* **77**, 2397–2399 (2000).
6. C. Zener, "Internal friction in solids, I: theory of internal friction in reeds," *Phys. Rev.* **52**, 230–235 (1937).
7. R. Lifshitz and M. L. Roukes, "Thermoelastic damping in micro- and nanomechanical systems," *Phys. Rev. B* **61**, 5600–5609 (2000).
8. A. H. Nayfeh and M. I. Younis, "Modeling and simulations of thermoelastic damping in microplates," *J. Micromech. Microeng.* **14**, 1711–1717 (2004).
9. S. J. Wong, C. H. J. Fox, and S. McWilliam, "Thermoelastic damping of the in-plane vibration of thin silicon rings," *J. Sound Vib.* **293**, 266–285 (2006).
10. A. Duwel, J. Gorman, M. Weinstein, J. Borenstein, and P. Ward, "Experimental study of thermoelastic damping in MEMS gyros," *Sens. Actuators, A* **103**, 70–75 (2003).
11. Z. L. Hao, "Thermoelastic damping in the contour-mode vibrations of micro- and nano-electromechanical circular thin-plate resonators," *J. Sound Vib.* **313**, 77–96 (2008).
12. Y. X. Sun and H. Tohmyoh, "Thermoelastic damping of the axisymmetric vibration of circular plate resonators," *J. Sound Vib.* **319**, 392–405 (2009).
13. M. J. Silver and L. D. Peterson, "Predictive elastothermodynamic damping in finite element models by using a perturbation formulation," *AIAA J.* **43**, 2646–2653 (2005).
14. D. J. Segalman, "Calculation of damping matrices for linearly viscoelastic structures," *J. Appl. Mech.* **54**, 585–588 (1987).
15. Y. B. Yi and M. A. Matin, "Eigenvalue solution of thermoelastic damping in beam resonators using a finite element analysis," *ASME J. Vibr. Acoust.* **129**, 478–483 (2007).
16. H. W. Tang, Y. B. Yi, and M. A. Matin, "Predictive modeling of thermoelastic energy dissipation in tunable MEMS mirrors," *J. Micro/Nanolith. MEMS MOEMS* **7**, 023004 (2008).
17. Y. B. Yi, "Geometric effects on thermoelastic damping in MEMS resonators," *J. Sound Vib.* **309**, 588–599 (2008).
18. Y. B. Yi, J. R. Barber, and P. Zagrodzki, "Eigenvalue solution of thermoelastic instability problems using Fourier reduction," *Proc. R. Soc. London, Ser. A* **456**, 2799–2821 (2000).
19. Y. B. Yi, "Finite element analysis on thermoelastodynamic instabilities involving frictional heating," *ASME J. Tribol.* **128**, 718–724 (2006).
20. S. Basak, A. Raman, and S. V. Garimella, "Hydrodynamic loading of microcantilevers vibrating in viscous fluids," *J. Appl. Phys.* **99**, 114906 (2006).
21. S. Inaba, K. Akaishi, T. Mori, and K. Hane, "Analysis of the resonance characteristics of a cantilever vibrated photothermally in a liquid," *J. Appl. Phys.* **73**, 2654–2658 (1993).
22. T. Naik, E. K. Longmire, and S. C. Mantell, "Dynamic response of a cantilever in liquid near a solid wall," *Sens. Actuators, A* **102**, 240–254 (2003).
23. S. K. De and N. R. Aluru, "Coupling of hierarchical fluid models with electrostatic and mechanical models for the dynamic analysis of MEMS," *J. Micromech. Microeng.* **16**, 1705–1719 (2006).
24. Z. L. Hao, R. Clark, J. Hammer, M. Whitley, and B. Wingfield, "Modeling air-damping effect in a bulk micromachined 2-D tilt mirror," *Sens. Actuators, A* **102**, 42–48 (2002).
25. W. T. Thomson and M. D. Dahleh, *Theory of Vibration with Applications*, Prentice Hall, Upper Saddle River, NJ (1997).
26. R. W. Fox, A. T. McDonald, and P. J. Pritchard, *Introduction to Fluid Mechanics*, 6th ed., Wiley, Hoboken, NJ (2006).
27. COMSOL, *Multiphysics 3.3 User's Manual*, COMSOL, Inc., Los Angeles, CA (2006).

Yun-Bo Yi received his PhD degree in mechanical engineering from the University of Michigan, Ann Arbor, in 2001. After four additional years of research work at the same institution, he joined the faculty at the University of Denver in 2005. He received his MS degree from the University of Missouri, Rolla, in 1997 and his bachelor's degree in automotive engineering from Tsinghua University, China, in 1994. Before he came to the United States, he worked at the Shanghai Automotive Research Institute for a year.

Amir Rahafrooz received his BSc in biomedical engineering from Isfahan University, Iran, in 2004, and his MSc in bioelectrics from Amirkabir University of Technology, Iran, in 2007. He is currently a PhD candidate in the Department of Electrical and Computer Engineering at the University of Denver, working under the supervision of Dr. Siavash Pourkamali in the NEMS lab. His research interests are mainly related to MEMS resonators and sensors as well as nano- and microrobots.

Siavash Pourkamali is an assistant professor in the Department of Electrical and Computer Engineering at the University of Denver. He received a BS degree in electrical engineering from Sharif University of Technology, Tehran, Iran, in 2001, and MS and PhD degrees in electrical engineering from the Georgia Institute of Technology, Atlanta, in 2004 and 2006, respectively. He joined the faculty at the University of Denver in 2006. His current research interests are in the areas of integrated silicon NEMS and nanosystems, nanofabrication technologies, nanomechanical resonant sensors, and nanorobotics for cellular and molecular biology.